# Direct Laser Synthesis of Functional Coatings by FEL treatments

Peter SCHAAF[*], Michelle SHINN[**], Ettore CARPENE[***], and Jörg KASPAR[****]

[*] *University of Göttingen, Zweites Physikalisches Institut, Friedrich-Hund-Platz 1, 37077 Göttingen, Germany*
*E-mail: pschaaf@uni-goettingen.de*
[**] *Thomas Jefferson National Accelerator Facility, Free Electron Laser Group, Newport News, VA 23606, USA*
[***] *Politecnico di Milano, Dipartimento di Fisica, piazza Leonardo da Vinci 32, 20133 Milano, Italy*
[****] *Fraunhofer Institut für Werkstoff- und Strahltechnik IWS, Winterbergstrasse 28, 01277 Dresden, Germany*

Smart surfaces and functional coatings play a decisive role for applicability and performance of all modern materials. Many methods have been developed for their fabrication. Recently, it was established that short laser pulses can induce a direct laser synthesis of functional coatings if the material's surface is irradiated in reactive atmosphere. Despite the simplicity of the treatment itself, the process is not yet industrially established, maybe due to the lack of high repetition rate high power pulsed lasers enabling fast and easy treatment of large areas and pieces. The Free Electron Laser (FEL) can be just the right tool to drive this process into applicability. The high power and the flexibility in temporal shaping of the FEL at the Jefferson Lab made it very interesting for direct laser synthesis of functional coatings. The produced coatings were investigated by a number or methods and the obtained results are presented in connection with the FEL treatment parameters. TiN coatings of about 15 µm thickness could be easily produced. Furthermore, (100) texturing of the TiN was found for certain timings of the FEL, which is explained by temperature and solidification modeling during the FEL irradiation.

DOI: 10.2961/jlmn.2006.02.0009

**Keywords:** Functional Coatings, Laser synthesis, nitriding, titanium, free electron laser, solidification processes.

## 1. Introduction

Titanium and its alloys play an important role in high load functional materials and also in biomedical applications. Regardless of the high cost of titanium and its alloys compared to steels, their low weight, their reliability under heavy working conditions and their low toxicity have promoted their application in several technological fields, ranging from aeronautic components to biomaterials [1]. However, titanium alloys have a rather poor wear resistance [2] and in order to improve their tribological properties, surface treatments are required. Besides the conventional gas and plasma nitriding, pulsed laser nitriding is an alternative way to enhance the surface features: it consists of the irradiation in controlled nitrogen atmosphere by means of a pulsed laser beam, allowing fast treatments and requiring no additional hardening due to the rapid cooling rates [3]. Laser nitriding of titanium and titanium alloys dates back to the eighties with the pioneering works of Katayama [4] and Ursu [5]. Since then, there have been a large number of publications on laser irradiation of titanium and its alloys in nitrogen gas, demonstrating the efficient nitrogen incorporation and the formation of nitride layers [6-11]. We report here the first results on laser nitriding of titanium substrates by means of a free-electron laser (FEL), which has never been employed before, and its main peculiarities being the high power and the adaptable temporal pulse-structure [12]. Particular emphasis is given to the analysis of the crystallographic texture and the mechanism leading to its development.

## 2. Experimental

Titanium samples (purity > 99.98%) of 1 mm thickness have been cut into square pieces of 15×15 mm$^2$ and mechanically polished with emery paper and diamond paste to 1 µm.

### 2.1 FEL treatment

The laser processing of the pure titanium substrates was performed with the infrared FEL at the Thomas Jefferson National Laboratory in Newport News (Virginia, USA). The FEL beam consisted of a sequence of 0.5-0.6 ps FWHM *micropulses* at a wavelength of 3.1 µm, an average micropulse energy $E_\mu$ = 20 µJ (corresponding to a pulse power $P_\mu$ = 40 MW) and a high repetition rate $f_\mu$=37.4 MHz. The duration $t_m$ of the ps pulse sequence could be set by the user in the range of 50-1000 µs, representing a so-called *macropulse*. The frequency $f_m$ of the macropulses could be varied from 10 Hz to 60 Hz. Thus, the energy delivered by one macropulse, $E_m = E_\mu f_\mu t_m$ could range from 0.04 J to 0.75 J, with an average power $P = E_m / t_m = E_\mu f_\mu$ = 750 W. The raw, Gaussian-like FEL beam of about 5 cm diameter was focused with a $CaF_2$ lens to a circular spot having a diameter of $D \approx 400$ µm. The corresponding macropulse fluence $\phi_m$ can be obtained as $4E_m/\pi D^2$ and is typically a few hundreds J/cm$^2$.

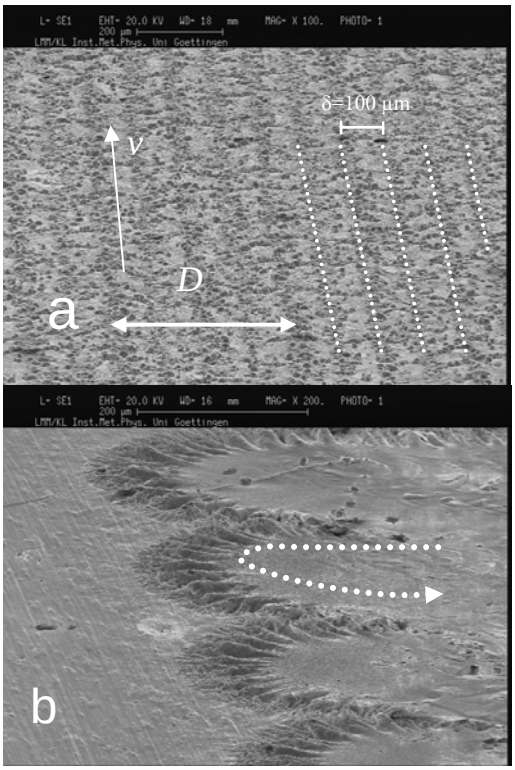


**Fig. 1** SEM micrographs of the titanium surface indicating the FEL laser treatment pattern: a) showing the scanning lines with

shift δ and b) the turning point with different morphology at the end of the scanning lines.

The samples were placed inside an irradiation chamber equipped with a fused silica window (absorbing about 20% of the incident energy) and filled with high purity nitrogen gas at 0.1 MPa. In order to treat a larger area, the chamber was mounted on a motorized, computer-controlled x-y table, allowing a meander scan of the Ti surface. The speed *v* of the sample, relative to the position of the laser beam was fixed to 0.5 mm/s and the lateral shift δ to 50, 100 or 200 µm, i.e. the sample has been moved along the x-axis at speed *v*, shifted by *d* along the y-axis, moved along the x-axis with speed -*v*, shifted again by δ along the y-axis, and so on. The resulting surface is sketched in Figure 1. The parameters for the most important samples are summarized in Table 1.

**Table 1** FEL treatment parameters of the samples (not all samples mentioned here).

| Sample | $t_m$ (µs) | $f_m$ (Hz) | $\delta$ (µm) | $\phi_m$ (J/cm$^2$) |
|---|---|---|---|---|
| Ti-a1 | 250 | 60 | 200 | 123 |
| Ti-a2 | 250 | 60 | 100 | 123 |
| Ti-a3 | 250 | 60 | 50 | 123 |
| Ti-b1 | 500 | 30 | 100 | 246 |
| Ti-c1 | 750 | 30 | 100 | 369 |
| Ti-d1 | 1000 | 10 | 200 | 492 |
| Ti-d2 | 1000 | 10 | 100 | 492 |
| Ti-d3 | 1000 | 20 | 200 | 492 |
| Ti-d4 | 1000 | 30 | 200 | 492 |
| Ti-d5 | 1000 | 30 | 100 | 492 |

### 2.2 Sample Analysis

The nitrogen content and depth profiles obtained after the laser treatment were measured (to a depth of about 400 nm) at the IONAS accelerator in Göttingen by Resonant Nuclear Reaction Analysis (RNRA) via the reaction $^{15}N(p,\alpha\gamma)^{12}C$ at the resonance energy of 429.6 keV [3].

The crystallographic phase analysis was carried out by means of x-ray diffraction (XRD) in Bragg-Brentano geometry and with rocking curve scans using a Bruker diffractometer with a Cu-$K_\alpha$ source.

The surface morphology was studied by scanning electron microscopy (SEM) at the Institute of Material Physics in Göttingen and at the Fraunhofer IWS in Dresden. Furthermore, cross sections of the layers were prepared by grinding and polishing. The polished specimens were chemically etched in a solution of 2 ml HF, 2 ml HNO3 and 96 ml H2O for a period of about 20 s. Further information about the structure and the spatial distribution of the phases formed were obtained in the SEM using backscattered electrons. To produce smooth, deformation free and sharp edged cross sections the metallographically prepared samples were ion beam polished in a Baltec RES010 ion beam etching system at low angles of incidence.

Additional analyses were performed by energy dispersive X-ray analysis (EDX) on cross-sections of the laser treated samples.

The microhardness depth profiles were measured with a Fischerscope HV100 nanoindenter equipped with a Vickers diamond tip, using a maximum load of and 1 N [3].

One measurement has been taken for each sample with the different methods. The experimental errors as a result of the analysis are given. In case of the nanoindenter, 25 measurements have been taken for each sample, and the error bars represent the error of the mean value.

## 3. Results and Discussion

At room temperature titanium exhibits an hcp cell (α-Ti, space group $P6_3/mmc$ [13]). According to the Ti-N equilibrium phase diagram [14], the nitrogen solubility in α-Ti can reach 23 at.% at about 1000°C, and it can exceed 50 at.% in the cubic phase (δ-$TiN_x$, B1-NaCl structure [13]); its lattice parameter *a* depends on the nitrogen fraction *x*: *a* [nm] = 0.41925 + 0.00467 *x* [15]). Other stable titanium nitrides are δ'-$Ti_2N$ and δ"-$Ti_2N$ (both having tetragonal structure [13]). Although some authors found enhanced surface hardness and wear resistance in the presence of the $Ti_2N$ phases [16–18], the difficulty in controlling their synthesis is considered as a major drawback for technical and industrial applications.

### 3.1 Compositional and Structural Results

Three typical nitrogen depth profiles as obtained by RNRA are reported in Fig. 2. Despite of the different FEL processing parameters ($f_\mu$ , $t_m$, δ), RNRA revealed that after the surface laser treatment the measured stoichiometry is always similar and at about 50 at.% N [18].

The nitrogen content slightly decreases with increasing depth, suggesting that the stoichiometry is not maintained over the whole thickness of the nitrided layer. This effect is most likely related to the diffusion nature of the nitrogen transport mechanism during the laser irradiation, as it has been established with excimer laser nitriding of other metals such as iron [19] and aluminum [20].

Information on the deeper nitrogen concentration could not be achieved by RNRA, since the maximum investigation depth of about 400 nm is limited by the maximum acceleration energy of the protons. Nevertheless, the technique is extremely sensitive to the stoichiometry, allowing a reliable estimate of the overall nitrogen content. It is worth to notice that RNRA enables to estimate the nitrogen concentration in the sample, regardless of its chemical state: nitrogen at the grain boundaries or in solid solution within the Ti matrix cannot be distinguished from nitrogen forming stoichiometric compounds.

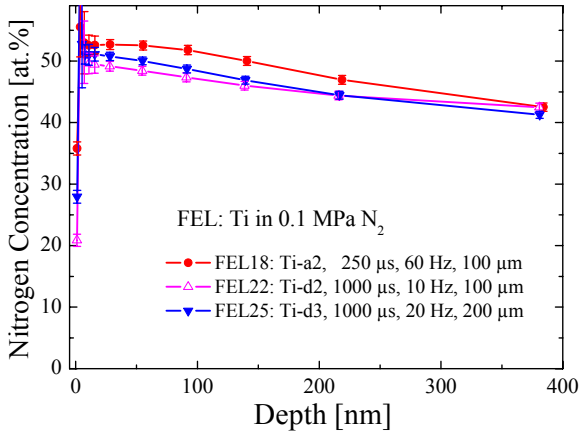


**Fig. 2** Nitrogen depth profiles as obtained by RNRA for three different treatment parameters (δ = 100 µm, $f_m$ , $t_m$ are given).

The nitrogen depth profile can be also obtained – with less accuracy - by EDX measurement at the cross section of the laser nitrided sample. An example is shown in Fig. 3. Also the absolute concentration is less accurate, the EDX depth profile clearly shows the diffusional origin of the nitrogen profile and it exhibits large nitriding depths of more than 20 µm.

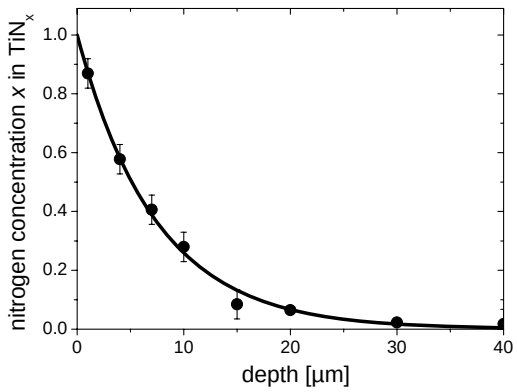


**Fig. 3** Nitrogen depth profile obtained by EDX for the sample treated with $\delta$=200 µm, $f_m$=20 Hz, $t_m$=750 µs. The data were normalized to match the RNRA result at the surface (RNRA is much more accurate).

The phase analysis of the irradiated samples was carried out by XRD. Figure 4 shows the Bragg-Brentano diffractograms of three selected specimens, revealing the formation of δ-$TiN_x$. The diffractograms also show the presence of α-Ti(N), but its abundance is always small compared to the amount of the cubic nitride. The diffractograms also show the presence of α-Ti(N) with a small (101) crystallographic texture. The positions of the Bragg peaks are slightly shifted to lower angles (i.e larger lattice parameters) compared to the values of pure α-Ti as a consequence of the nitrogen incorporation. However, the underlying pure titanium substrate could contribute as well to these peaks, and any estimate of the nitrogen fraction from the values of the lattice parameters would be unrealistic.

From the relative intensities of the Bragg peaks, a pronounced δ-$TiN_x$ (200) crystallographic texture could be inferred, especially in the samples treated with the lowest macropulse frequency $f_m$ and the longest pulse duration $t_m$.

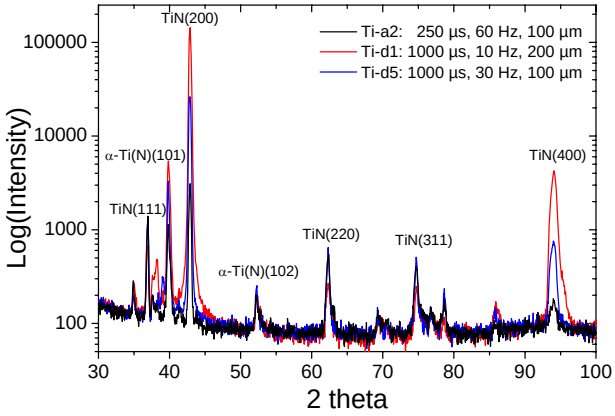


**Fig. 4** Diffractograms obtained in Bragg-Brentano geometry for three typical samples treated with different FEL parameters.

To quantify this effect, rocking curves of the δ-$TiN_x$ (200) Bragg reflection, of which some examples are reported in Fig. 5, were performed. The correlation between the macropulse frequency $f_m$ and the full width at half maximum (FWHM) of the δ-$TiN_x$ (200) rocking peaks is displayed in Fig. 6 for the samples treated with a macropulse duration $t_m \geq 750$ µs (for lower $t_m$ values the width of the rocking peak cannot be unambiguously determined, i.e. the texture is weak or absent).

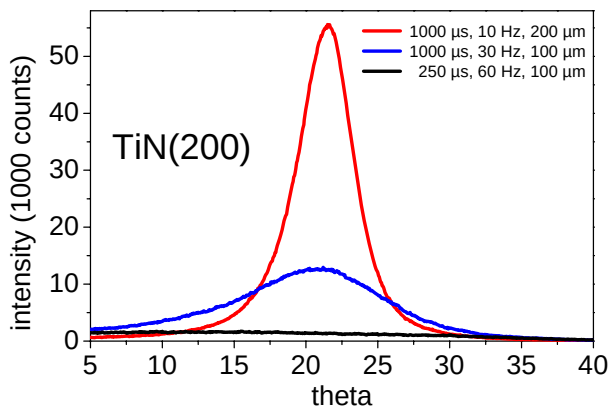


**Fig. 5** Rocking curves of the (200) TiN reflexes. Parameters are given in the graph.

It is worth noting that the degree of crystallographic texture increases with decreasing pulse frequency, i.e. with decreasing spot overlap, suggesting that the texture better develops with fewer macropulses hitting the same surface area.

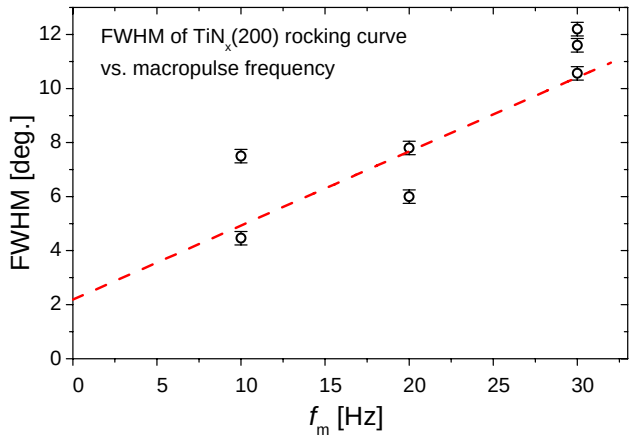


**Fig. 6** Width of the (200) rocking curves of TiN as a function of the macropulse frequency (FWHM).

From the symmetric Bragg-Brentano scans and the rocking curves of the textured samples it is possible to conclude that the $TiN_x$(200) planes are preferentially oriented parallel to the sample surface, However, nothing can be said about the preferential orientation of crystallographic planes not parallel to the surface. This information can only be obtained from pole figures. This is seen nicely in the pole figure of the TiN peaks presented in Fig. 7. It clearly evidences a fiber texture with (200) orientation. The (111) pole figure seems to have a slightly weaker intensity along the horizontal line, which might be caused by the scanning direction having the same orientation.

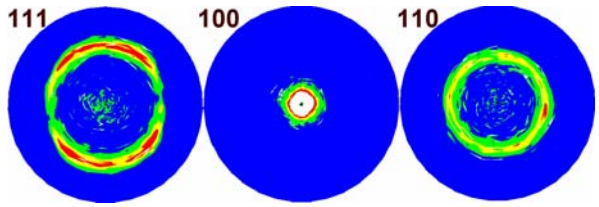


**Fig. 7** Pole figures of the three prominent TiN reflexes for the sample treated with $\delta$=200 µm, $f_m$=20 Hz, $t_m$=750 µs (same as in Fig. 3).

The detailed analysis of the XRD spectra has disclosed not only the influence of the macropulse frequency, but also of the lateral overlap on the crystallographic texture of the δ nitride. In an ideal polycrystalline δ-TiN powder the ratio between the intensities of the $TiN_x$(111) and the $TiN_x$(200) Bragg peaks should be 0.72 [18]. We term this ratio as the *texture parameter* $\eta = I_{111}/I_{200}$. A value $\eta \ll 0.72$ indicates a strong (100) texture, while $\eta = 0.72$ would correspond to perfect polycrystal. We also define the *laser spot overlap parameter* $\sigma$ as follows: since the relative velocity $v$ of the laser beam with respect to the sample has been fixed during the irradiation, the higher is the macropulse frequency $f_m$, the bigger is the spot overlap in the direction of motion. On the other hand, the larger is the lateral displacement $\delta$, the smaller is the lateral overlap. Therefore we can write $\sigma = D^2 f_m/(v\delta)$, with $D$ being the laser spot diameter. The qualitative correlation between the crystallographic texture and the spot overlap is shown in Fig. 8, where both σ and η are plotted for all the samples considered in this work.

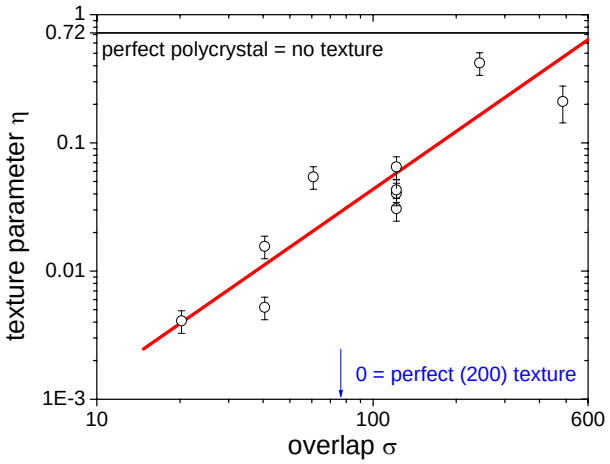


**Fig. 8** Correlation between texture parameter $\eta$ and overlap $\sigma$. For details see text.

On the basis of the columnar growth model, we can conclude that the high spot overlap tends to hinder the formation of columnar grains. With high macropulse frequency and small lateral displacement the laser spots get closer to each other. Convection in the melt, as well as effects of the spot edges become more important, misaligning or even disrupting the columnar grains, and leading to the formation of a polycrystalline layer. For low spot overlap, these effects are less pronounced and well-aligned columnar grains can develop.

The angular positions of the $TiN_x$(200) and $TiN_x$(400) Bragg peaks have been used to estimate the average lattice parameter $a_{TiN}$ of the δ phase. The analysis has shown a rather wide scatter of the data with 0.4209 nm < $a_{TiN}$ < 0.4218 nm, however, no simple correlation with the irradiation conditions could be found. Since the lattice parameter is correlated to the nitrogen fraction $x$ by the relation $a(x)$ = 4.1925 +0.0467 $x$ [15], the average nitrogen concentration $c_N$ in the $TiN_x$ phase can be computed as $c_N=x/(1+x)$, obtaining values ranging from 25.8 at.% to 35.2 at.%. These values are smaller than those obtained by RNRA, but it should be taken into account that the X-ray information depth in Ti and TiN exceeds 5 µm and therefore the effect of concentration gradients is more pronounced. Besides, the nitrogen at the grain boundaries is invisible to the XRD technique, although it is contributing to the RNRA spectra.

The morphology of the sample surfaces after the laser treatment has been investigated by SEM. Fig. 9 reports the surface micrographs of four selected samples. Similar to the correlation between the macropulse duration and the crystallographic texture, the differences in the surface morphology could also be the ascribed to the length of the laser pulse. With high spot overlap and short macropulse duration a very rough surface is formed (Fig. 9a) with spherical-like structures of 5-20 µm in diameter, homogeneously distributed over the whole irradiated area. It is worth mentioning that this sample is almost texture-free.

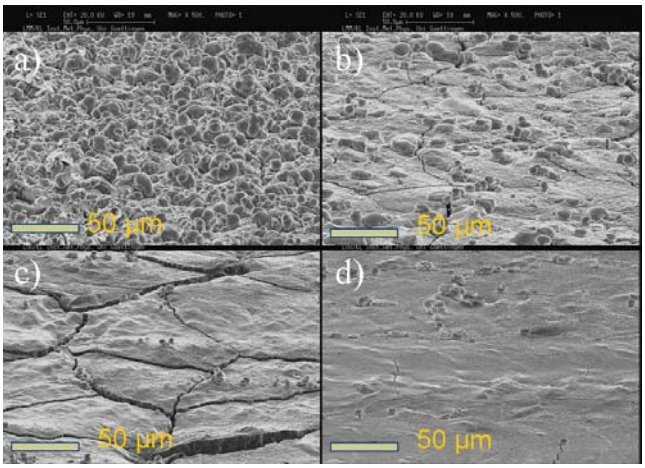


**Fig. 9** SEM pictures from the surfaces of the laser nitrided titanium: a) $\delta$=100 µm, $f_m$=60 Hz, $t_m$=250 µs, b) $\delta$=100 µm, $f_m$=30 Hz, $t_m$=750 µs, c) $\delta$=100 µm, $f_m$=30 Hz, $t_m$=1000 µs, d) $\delta$=200 µm, $f_m$=10 Hz, $t_m$=1000 µs.

With intermediate spot coverage and longer pulse length, the density of these spherical structures drastically decreases, revealing the rather smooth underlying surface (Fig. 9b and 9c). Some cracks become visible (especially in the sample treated with 1000 µs macropulse duration) forming "plates" of 50-100 µm in dimension. With the smallest spot overlap (Fig. 9d), the spherical structures disappear almost completely, the dimension and density of cracks is visibly reduced and a very uniform surface is formed. This last sample has also the strongest $TiN_x$ (200) texture. According to the microscopic investigation it seems that the roughness/homogeneity of the treated surface is in good agreement with the crystallographic observations: rough surfaces reveal no crystallographic orientation, while homogeneous and uniform surfaces (plates) correspond to the sharpest crystallographic texture.

To clarify what caused the crystallographic texture, we performed cross-sectional SEM.

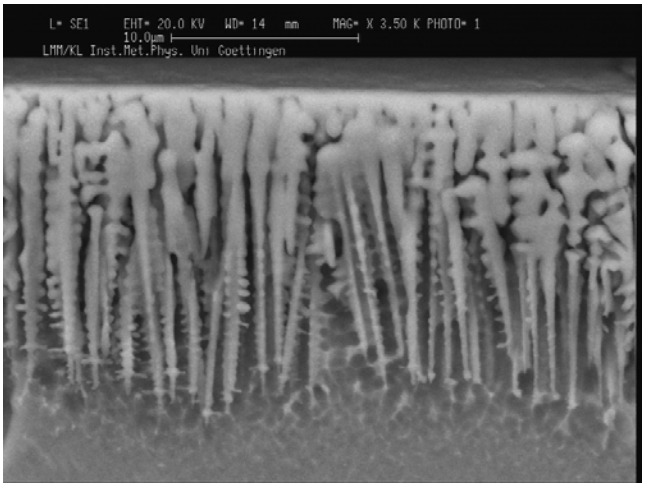


**Fig. 10** Cross-section micrograph (SEM) for the sample treated with $\delta$ =200 µm, $f_m$=20 Hz, $t_m$=750 µs.

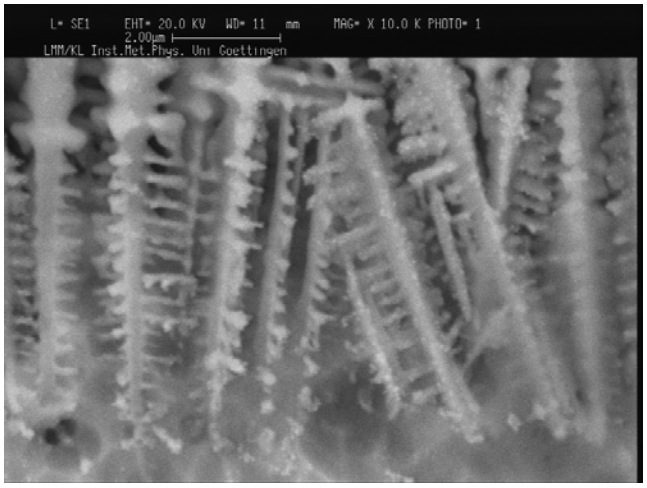


**Fig. 11** Cross-section micrograph (SEM) for the sample treated with $\delta$ =200 µm, $f_m$=20 Hz, $t_m$=750 µs.

The cross-sectional micrographs reported in Fig. 10 and 11 refers to one of the samples with high degree of $TiN_x$ (200) texture. The dendritic region extends from the surface to a depth of roughly 10-15 µm and is formed by well-aligned δ-$TiN_x$ dendrites normal to the surface. This observation reveals the origin of the crystallographic texture: it is well known that the dendrites typically grow along the (100) crystallographic direction in cubic materials like TiN [15]. The tips of the dendrites pointing towards the bulk indicate that their growth began at the surface. Similar structures have been observed after $CO_2$ laser nitriding of a Ti-6Al-4V alloy, and it has been suggested that the solidification could occur from the surface [9]. However, no correlation with the crystallographic features of the samples and no quantitative interpretation supporting the solidification behavior have been given.

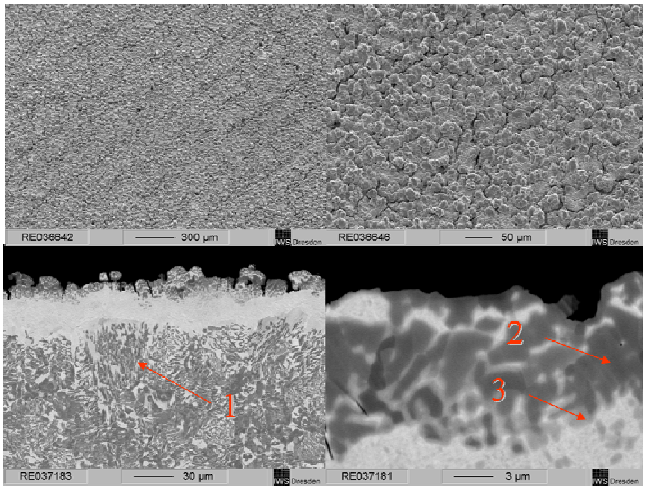


**Fig. 12** Surface (top) and cross-section (bottom) as seen in SEM for the sample treated with $\delta$=100 µm, $f_m$=60 Hz, $t_m$=250 µs. EDX reveals the nitrogen concentration at point 1: 8 at.%, 2: 23 at.%, 3: 16 at.%.

The SEM pictures in Fig. 12 confirm the previous findings showing the very rough surface with many melting pearls and a network of fine cracks. The melting depth is about 30-40 µm, with a TiN thickness of about 5-15 µm. One recognizes a primary solidification of TiN at the surface. The TiN grains have a nitrogen rich kernel and less nitrogen in their shell. α'-martensite is found between the TiN grains.

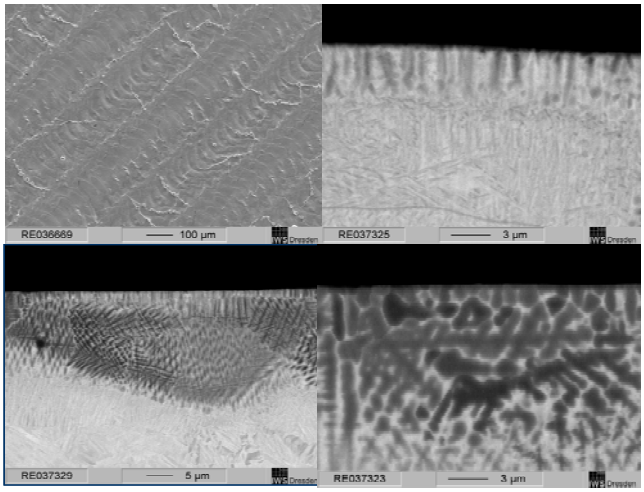


**Fig. 13** Surface (top left) and cross-sections as seen in SEM for the sample treated with $\delta$=200 µm, $f_m$=10 Hz, $t_m$=1000 µs. EDX reveals nitrogen concentrations of 30 at.% in the dendrites and about 10 at.% in between.

The SEM micrographs in Fig. 13 reveal the microstructure and morphology of a highly textured sample. The melting zone is 20-30 µm and the TiN amounts up to 0-25 µm. We see a very smooth surface with very few melt pearls. Significant solidification lines are visible and few fine cracks appear. Cracks are only seen within TiN. The nitrogen poor shell of the TiN is smaller than for the non textured sample. The dendritic solidification growing from the surface and perpendicular to it is obvious.

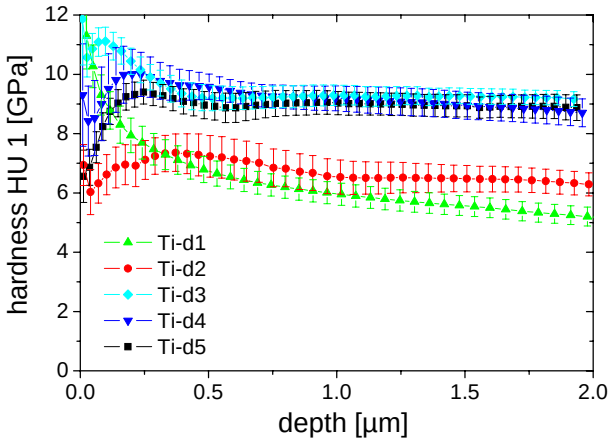


**Fig. 14** Hardness depth profiles obtained by nanoindentation.

The mechanical properties of the FEL-nitrided titanium samples have been investigated by nanoindentation using a load of 1 N. The specimens with very rough surface exhibited a large scatter of the hardness values and a reliable estimate could not be achieved. For the other samples, the indentation points have been carefully chosen in order to avoid cracks or inhomogeneities of the surface (typically close to the edges of the irradiated area, as seen in Fig. 1b). The results of the nanoindentation tests are reported in Fig. 14. The surface hardness varies between 6 and 12 GPa, depending on the parameters of irradiation. A rather constant hardness profile is observed for the samples treated with high spot overlap (Ti-d3, Ti-d4 and Ti-d5), while stronger decrease of the hardness with increasing depth characterizes the samples treated with low spot coverage (Ti-d1 and Ti-d2). We noticed that the crystallographic texture does not determine any enhancement of the surface hardness. On the contrary, the sample with the highest texture parameters (Ti-d1) is also the one with the steepest hardness decrease. The deterioration of the hardness profile might be more severely influenced by nitrogen content rather than the crystallographic characteristics of the samples. We have already observed a

direct correlation between the surface hardness and the nitrogen content in iron [3] and in aluminum [20] samples nitrided by an excimer laser. Assuming that the same phenomenon occurs in FEL-nitrided titanium, the decrease of the hardness profile suggests the existence of a nitrogen concentration gradient that is reasonable to expect in the samples treated with low spot overlap, i.e. few macropulses per area. This is confirmed by the EDX results.

### 3.2 Temperature and Solidification Modeling

With the help of numerical simulations we can now provide an explanation. The melting point of $TiN_x$ is a monotone function of the nitrogen fraction $x$, with its minimum at $x = 0$ (1941 K [16]) and its maximum at $x = 1$ (3220 K [16]). An inhomogeneous nitrogen depth profile accordingly introduces a depth-dependent melting point. Our numerical simulation indicates that in the presence of a nitrogen concentration gradient, the sample surface solidifies while the underlying bulk is still molten. The simulation has been based on the finite-difference numerical solution of the 3-dimensional heat transport equation (in cylindrical coordinates):

$$\rho \frac{\partial H}{\partial t} = \nabla \cdot \left( \kappa \cdot \nabla T \right) + \alpha \cdot e^{-\alpha z} \left( 1 - R \right) I \left( r, t \right). \quad (1)$$

The quantities $\rho$, $H$ and $\kappa$ are the density, the heat per unit mass and the thermal conductivity of the material, respectively, $T$ is the local temperature, $R$ and $\alpha$ are the optical reflectivity and the absorption coefficient at the wavelength of 3.1 µm, $I(r,t)$ is the space and temporal dependence of the laser irradiance, $z$ and $r$ are the axial (normal to the surface) and the radial (parallel to the surface) coordinates, respectively. The quantity (1-$R$) represents the fraction of the laser irradiance that is absorbed by the sample: for Ti and TiN in the infrared spectral region, it is about 20% [21-28]. The analytical solution of Eq.(1) can be found only in very special cases, and normally a numerical approach is used. However, even the numerical solution requires the knowledge of all thermophysical parameters, which in general are functions of the temperature and the composition of the material. Since these parameters are known only for pure Ti and TiN, in the intermediate nitrogen atomic fraction $0 < x < 1$ they were calculated as the average, weighted by $x$: $A(x) = xA_{TiN} + (1-x)A_{Ti}$, with $A_{TiN}$ and $A_{Ti}$ being the generic thermophysical quantities of TiN and Ti, respectively, and $A(x)$ the parameter of the non-uniform medium. For a given nitrogen depth profile, the atomic fraction $x$ was simply substituted by $x(z)$. For simplicity, we neglected the nitrogen transport during the laser irradiation (in other words, we assumed zero-diffusion of nitrogen in titanium). The solid/liquid phase transition was considered in the heat transport equation by including the latent heat of melting $L_m$ in the definition of $H$, while the energy flux due to the evaporated material was calculated by means of the Hertz-Knudsen equation as a surface boundary condition [16,21]. The thermal conductivity $\kappa$ and specific heat $c_p$ of Ti and TiN were assumed temperature-independent parameters obtained from the average values found in literature [17,22-28]. Fig. 15 reports the numerical simulations performed with pulse duration of 750 µs and a beam power of 750 W focused on a circle of 400 µm in diameter.

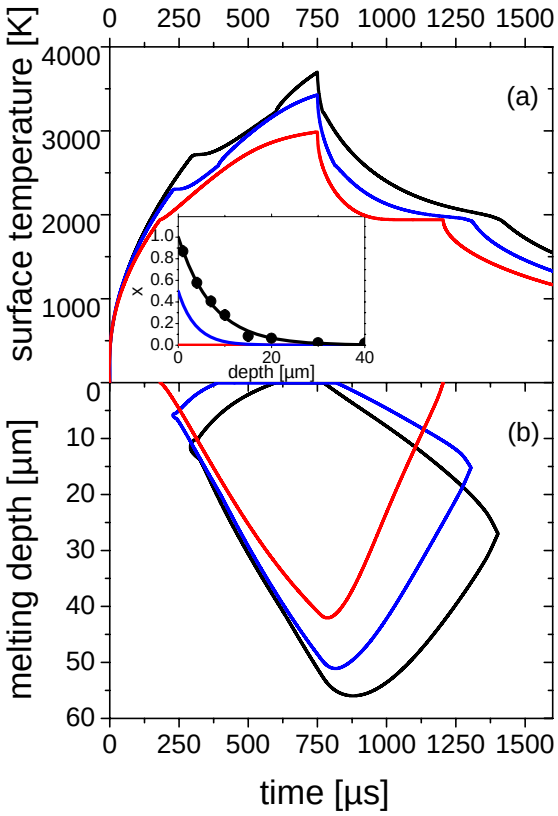


**Fig. 15** The numerical simulations show the temporal evolution of the surface temperature (a) and melting depth (b) in the center of the irradiated area, assuming a pulse duration of 750 µs and a laser power of 750 W on a circular spot of 400 µm in diameter. Three nitrogen depth profiles, reported in the inset, have been considered in the calculations (the red line corresponds to pure Ti); the solidification occurs from the surface only in the presence of a nitrogen concentration gradient. The dots in the inset are the experimental nitrogen depth profile measured by EDX in the sample shown in Fig. 3 and 10, prior to the etching.

Fig. 15a shows the evolution of the surface temperature in the center of the laser spot for the three different nitrogen depth profiles reported in the inset. Fig. 15b represents the evolution of the melting depth in the center of the irradiated area, revealing that only in the presence of a nitrogen concentration gradient, the solidification occurs at the surface while the bulk is still molten. This leads to the interesting result, that the surface can be solid and we have a molten layer below, or in other words, melting starts in deeper layer and not at the surface. These results agree with the morphology of the dendritic surface region observed by SEM. The development of the crystallographic texture is a consequence of the strong dendritic alignment, and the fact that the dendrites grow with their [100] axis normal to the surface might be related to the surface energy of δ-TiN. Based on the Density Functional Theory (DFT), the static energies of the (100), (110) and (111) TiN planes have been calculated, obtaining the quantitative relation S100 : S110 : S111 = 1:53 : 2:87 : 5:0822.

This demonstrates that the TiN(200) surface is the most stable one. Since the solidification takes place from the surface, TiN(200) planes arrange parallel to the sample surface and, as the sample cools, the grains (i.e. dendrites) grow, maintaining this crystallographic orientation. When the spot overlap is too strong (i.e. high macropulse frequency) convection in the melt might hinder the dendrites' alignment and the crystallographic texture. Besides, short macropulses ($t_m$ < 500 µs) do not deliver enough energy to melt the surface (see Fig. 15b) and the textured growth cannot develop.

## 7. Conclusions

In conclusion, the free-electron laser has been employed successfully, for the first time to process titanium in nitrogen gas. The formation of

δ-TiN coatings has been revealed and related to the experimental parameters: the development of a sharp crystallographic texture correlates with the existence of a solidification front moving from the surface towards the bulk, allowing the formation of a well-aligned dendritic region. This unusual solidification behavior is induced by the inhomogeneity of the chemical composition (i.e. the nitrogen concentration gradient) and by the resulting thermophysical features of the material. There is a whole class of compounds thermodynamically and crystallographically similar to the Ti-N system that should behave accordingly under FEL irradiation: TiC, $TiC_xN_{1-x}$, ZrN, ZrC and TaN, just to mention a few with technological applications. Furthermore, the strong adaptability of the free-electron laser suggests that a proper tuning of the experimental parameters can enhance the processing speed by 2-3 orders of magnitude. We believe these results should stimulate research in the field of laser synthesis with particular emphasis on the development of microstructures, which might have a high technological impact for light-weight alloys and advanced biomaterials.

**Acknowledgments**

This work is supported by the Deutsche Forschungsgemeinschaft (DFG) under grant Scha 632/4. The Jefferson Lab is supported by the U.S. Dept. of Energy, the Office of Naval Research, the Commonwealth of Virginia and the Laser Processing Consortium. Kevin Jordan and Joseph F. Gubeli III are gratefully acknowledged for their kind and expert assistance at the FEL.

**References**

[1] C. Leyens, M. Peters (Eds.): Titanium and Titanium Alloys: Fundamentals and Applications (Wiley-VCH, Weinheim, 2003).
[2] K. G. Budinski: Wear **151** (1991) 203.
[3] P. Schaaf: Prog. Mater. Sci. **47** (2002) 1
[4] S. Katayama, A. Matsunawa, A. Morimoto, S. Ishimoto, Y. Arata: J. Metals **35** (1983) 85
[5] I. Ursu, N. Mihailescu, A. M. Prokhorev, V. I. Konov, V. N. Tokarev, S. A. Uglov: J. Phys. D: Appl. Phys. **18** (1985) 2547.
[6] E. D'Anna, G. Leggieri, A. Luches, M. Martino, A. V. Drigo, I. N. Mihailescu, G. Ganatsios: J. Appl. Phys. **69** (1991) 1687.
[7] V. M. Weerasinghe, D. R. F. West, J. de Damborenea: J. Mat. Proc. Tech. **58** (1996) 79.
[8] A. L. Thomann, C. Boulmer-Leborgne, C. Andreazza-Vignolle, P. Andreazza, J. Hermann, G. Blondiaux: J. Appl. Phys. **80** (1996) 4673.
[9] C. Hu, T. N. Baker: J. Mater. Sci. **32** (1997) 2821.
[10] S. Ettaqi, V. Hays, J. J. Hantzpergue, G. Saindrenan, J. C. Remy: Surf. Coat. Tech. **100** (1998) 428.
[11] J. C. Mori, P. Serra, E. Martinez, G. Sardin, J. Esteve, J. L. Morenza: Appl. Phys. A **69** (1999) S699.
[12] G. R. Neil, L. Merminga: Rev. Mod. Phys. **74** (2002) 685.
[13] International Centre for Diffraction Data, Powder Diffraction File database PDF-2: files 44-1294 (α-Ti), 38-1420 (δ-TiN), 23-1455 (δ-Ti2N) and 17-0386 (ε-Ti2N)
[14] J. M. Molarius, A. S. Korhonen, E. O. Ristolainen: J. Vac. Sci. Technol. A **3** (1985) 2419.
[15] M. Van Stappen, K. De Bruyn, C. Quaeyhaegens, L. Stals, V. Poulek: Surf. Coat. Technol. **74** (1995) 143.
[16] S. M. Johns, T. Bell, M. Samandi, G. A. Collins: Surf. Coat. Technol. **85** (1996) 7.
[17] A. Matthews: J. Vac. Sci. Technol. A **3** (1985) 2354.
[18] E. Carpene, M. Shinn, P. Schaaf: Appl. Surf. Sci. (2005) in print.
[19] E. Carpene, F. Landry, P. Schaaf: Appl. Phys. Lett. **77** (2000) 2412.
[20] E. Carpene, P. Schaaf: Phys. Rev. **B 65** (2002) 224111.
[21] W. Kurz, D. J. Fisher: Fundamentals of Solidification (Trans Tech Publications Ltd, Switzerland, 1998).
[22] Landolt-Börnstein: Numerical Data and Functional Relationships in Science and Technology, New Series, Vol.IV/19A (Springer, Heidelberg 2001). The thermophysical data used to describe the solid/liquid phase transition are: $T_m$(Ti) = 1941 K, $T_m$(TiN) = 3220 K, $L_m$(Ti) = 18 kJ/mol and $L_m$(TiN) = 67 kJ/mol; the enthalpy $\Delta H_v$ and entropy $\Delta S_v$ of vaporization used in the Hertz–Knudsen equation are: $\Delta H_v$(Ti) = 473 kJ/mole, $\Delta S_v$(Ti) = 150 J/mole K, $\Delta H_v$(TiN) = 809 kJ/mole, $\Delta S_v$(TiN) = 193 J/mole K.
[23] R. C. Weast, M. J. Astle (Eds.): Handbook of Chemistry and Physics (CRC Press, Boca Raton, Florida 1982, 63rd edn.)
[24] B. Karlsson, R. P. Shimshock, B. O. Seraphin: Solar Energy Mater. **7** (1983) 401.
[25] M. von Allmen, A. Blatter: Laser-Beam Interactions with Materials (Springer, Berlin, 1998).
[26] M. I. Aivazov, A. K. Muranevich, I. A. Domashnev: High Temperature **7** (1969) 830. We used κ(Ti) = 0.25 W/(cm K), κ(TiN) = 0.20 W/(cm K).
[27] Y. S. Touloukian, C. Y. Ho (eds.): Thermophysical Properties of Matter, Vol. 1 and 4 (Plenum Press, New York 1970). We used $c_p$(Ti) = 0.6 J/(g K) and $c_p$(TiN) = 0.8 J/(g K).
[28] M. Marlo, V. Milman: Phys. Rev. B **62** (2000) 2899.

(Received: April 28, 2005, Accepted: May 10, 2006)